

AB-INITIO PULSAR MAGNETOSPHERE

ALEXANDER A. PHILIPPOV¹, ANATOLY SPITKOVSKY

Department of Astrophysical Sciences, Princeton University, Ivy Lane, Princeton, NJ 08540
 Draft version May 15, 2017

ABSTRACT

We perform particle-in-cell simulations of pulsar magnetospheres, including pair production, ion extraction from the surface, frame dragging corrections, and high energy photon emission and propagation. In the case of oblique rotators, effects of general relativity significantly increase the fraction of open field lines which support the active pair discharge. We find that plasma density and particle energy flux in the pulsar wind is significantly non-uniform with latitude. Significant fraction of the outgoing particle energy flux is carried by energetic ions, which are extracted from the stellar surface. Their energies may extend up to a significant fraction of the open field line voltage, making them interesting candidates for ultra high-energy cosmic rays. We show that pulsar gamma-ray radiation is dominated by synchrotron radiation, emitted by particles which are energized by relativistic magnetic reconnection close to the Y-point and in the equatorial current sheet.

Subject headings: plasmas – pulsars: general – stars: magnetic field – stars: rotation

1. INTRODUCTION

Significant progress has been made in global PIC modeling of pulsar magnetospheres. It was shown how the magnetospheric configuration changes between the charge-separated disk-dome configuration to the plasma-filled state, close to the force-free solution (Philippov and Spitkovsky 2014; Chen and Beloborodov 2014; Belyaev 2015; Cerutti *et al.* 2015; Philippov *et al.* 2015a), under sufficient plasma supply from pair discharges. The effects of general relativity were shown to play an important role in establishing the pair production in aligned pulsars (Philippov *et al.* 2015b; Gralla *et al.* 2016; Belyaev and Parfrey 2016). Preliminary studies of nearly force-free magnetospheres showed an important role of the current sheet beyond the light cylinder for particle acceleration and emission of high-energy photons (Cerutti *et al.* 2016).

In this paper we present GR simulations of oblique rotators, which include pair production by magnetic conversion of photons and by photon-photon collisions. We discuss the magnetospheric structure, particle acceleration, modeling of the high-energy emission and implications for the structure of the pulsar wind.

2. NUMERICAL METHOD

Our simulations are performed using 3D relativistic PIC code TRISTAN-MP. Our basic setup follows Philippov *et al.* (2015a) with a few modifications. Inside the star, we force the fields to known values with a smoothing kernel. The magnetic field in the star is set to the field of a rotating dipole $\vec{B} = (3\vec{r}(\vec{\mu} \cdot \vec{r}) - \vec{\mu})/r^3$, where $\vec{\mu}(t) = (\cos(\Omega_* t) \sin \alpha, \sin(\Omega_* t) \sin \alpha, \cos \alpha)$ is the magnetic moment vector, and α is the inclination angle. Electric field inside the sphere is forced to corotation values $\vec{E} = -(\vec{\Omega}_* - \omega_{LT}) \times \vec{r} \times \vec{B}$, where ω_{LT} is the Lense-Thirring angular velocity (see below). At the distance of $4R_{LC}$ from the star, we apply the absorbing layer boundary condition (Cerutti *et al.* 2015), which mimics the

outflow condition for both fields and particles.

Philippov *et al.* (2015a) showed that the effects of frame-dragging are of crucial importance for efficient pair production over a significant area of the polar cap. In order to take them into account, we modified the Maxwell solver of TRISTAN-MP and added a new term into Faraday's induction equation, which describes the generation of electric field due to the rotation of space-time:

$$\frac{1}{c} \frac{\partial \vec{B}}{\partial t} = -\nabla \times \left(\vec{E} + \frac{\vec{\beta}}{c} \times \vec{B} \right), \quad (1)$$

where $\vec{\beta} = \frac{1}{c} \vec{\omega}_{LT} \times \vec{r}$ and $\omega_{LT} = \frac{2}{5} \Omega_* \frac{r_g}{R_*} \left(\frac{R_*}{r} \right)^3$ (for details, see Philippov *et al.* 2015b). Since frame-dragging is important only close to the stellar surface, the magnetic field in the RHS of (1) can be considered to be dipolar. As was shown in Philippov *et al.* 2015a; Belyaev and Parfrey 2016; Gralla *et al.* 2016, this is the only term, which needs to be taken into account. All our simulations are performed for the compactness value of $r_g/R_* = 0.5$.

As previously, we consider two sources of plasma supply in the magnetosphere: extraction of particles from the stellar surface based on the value of local surface charge, similar to Philippov *et al.* (2015a), and pair creation. Below positively charged particles coming from the surface are referred to as ions. For simplicity, we consider them to have the same charge to mass ratio as electrons. However, they are not allowed to participate in the pair production process and do not experience radiation reaction force. In this paper, we consider two sources of pair production: magnetic conversion and the two-photon decay. The first channel operates near the star, at $r < 2R_*$. We model the magnetic conversion in a way described in Philippov *et al.* (2015b): a new pair is injected whenever the energy of a simulation particle exceeds the threshold value, $\gamma > \gamma_{min}$, which is set to $\gamma_{min} = 0.01\gamma_0 = 20$, where γ_0 is the Lorentz factor of a particle experiencing the full vacuum potential drop between the pole and the equator, $\gamma_0 = (\Omega_* R_*/c)(B_0 R_*/c^2) \approx 2000$ in simulation. The

¹ sashaph@princeton.edu

polar cap voltage, Φ_{PC} , corresponds to possible particle acceleration up to Lorentz factors $\gamma_{PC} = (\Omega_* R_*/c)\gamma_0 = 500$. The second channel mimics collisions of the high-energy photons. Photons are emitted by energetic particles via synchrotron mechanism. Their frequency is set as $eB_{eff}\gamma^2/m_e c = e\sqrt{(\vec{E} + \vec{v} \times \vec{B}/c)^2 - (\vec{v} \cdot \vec{E}/c)^2}\gamma^2/m_e c$ (Cerutti *et al.* 2016), where \vec{v} and γ are the velocity and Lorentz factor of the emitting particle. Momentum of the emitted photon is set to be along the direction of motion of the energetic particle. For each photon, we assign the mean free path, which scales with the local density of photons n_γ^{-1} , such that the typical mean free path of photons at the light cylinder is $L_{mfp} = 0.5R_{LC}$. We performed simulations with different values of L_{mfp} and report our results below.

3. PULSAR MAGNETOSPHERE

3.1. Magnetospheric structure

After one rotation period, solution approaches a steady-state in the corotating frame. We show the field structure and densities of different species in the magnetosphere of 60° rotator in Figure 1. The magnetic field structure is similar to the force-free solution and PIC simulation in flat space-time presented in (Philippov *et al.* 2015a). Compared to our earlier simulations in flat space-time (Philippov *et al.* 2015a), we find that inclusion of GR effects significantly increases the number of pair producing field lines, see Figure 1a and b. However, as in the case of the aligned rotator, some field lines still carry the sub-GJ current, which is supported by the charge-separated outflow of electrons. In the case of 60° rotator, these field lines are located around the null current line $j_{\parallel} = 0$. In addition to the polar cap zone, we observe pair production in the return current layer and in the equatorial current sheet. These regions are highlighted by the distribution of high-energy photons in the magnetosphere (Figure 1c). The voltage drop in the return layer is non-uniform, so that pair production mostly takes place near the stellar surface and close to the Y-point. We note that for lower inclinations the return layer is more efficient photon emitter (for example, see photon density in the magnetosphere of 30° inclined pulsar in Figure 3.1). However, for all inclinations, the current sheet beyond the Y-point is the most significant source of high-energy photons and pairs in the outer magnetosphere. Plasma in the closed field region is mostly charge-separated and dominated by ions (see Figure 1d). Ions are extracted from the star with small momentum and travel along the dipolar field line until they hit the star. Ions are also pulled off the surface in the return current regions and are accelerated to high energies in the magnetospheric current sheet, see discussion below. In the case of significant mean free path of photons, we observe pair plasmas at some closed field lines. These pairs are produced by photons which propagate back to the star and are emitted close to the Y-point. Pairs on closed field lines travel along field lines until they hit the stellar surface.

Earlier simulations of magnetospheres with pair production (Chen and Beloborodov 2014; Philippov *et al.* 2015b) found the formation of a density gap above the current sheet. We find that if the photon mean free path becomes comparable to the light cylinder, this gap starts

to be filled with plasma, produced in the decay of photons emitted by energetic particles in strong current layers. However, we do not observe a subsequent discharge from the freshly produced pairs, so the density of pairs remains significantly lower compared to the dense polar outflow and current layers. This is because the available voltage on these field lines is significantly smaller compared to the voltage in strong current sheets.

Pair production at high altitudes is supported by the two-photon decay. We find that region around the Y-point produces most of the simulation photons. As shown in Figure 3.1, the region near the light cylinder also supports a counter-streaming photon distribution. We find that the backward propagating photons are emitted mostly by electrons, which were captured by the current sheet and reversed by the electric field. The outgoing photons near the Y-point are mostly produced by the escaping positrons², which come from the return layer or the wind. Counter-streaming photon flows are highly favorable for pair production. Lyubarskii (1996) was the first to estimate the pair production efficiency in the current sheet. This analysis can be improved by taking backward propagating photons into account.

We observe the equatorial current sheet to be unstable to both drift-kink and tearing instabilities. Plasmoids, which are produced by tearing instability of the current sheet, can be clearly seen in the equatorial plane, where the dominant reconnecting component of the magnetic field B_ϕ is in plane. They are also noticeable in three-dimensional current density distribution, as shown in Figure 4. The drift-kink instability mostly disappears at high inclinations (see the difference in the current sheet shape in Figure 1 and Figure 3.1), since $\nabla \times \mathbf{B}$ is supported mainly by the displacement current.

3.2. Particle acceleration

Near the star, particles are accelerated in regions of super-GJ current $j_{\parallel}/j_{GJ} > 1$ and in the return current layer, where $j_{\parallel}/j_{GJ} < 0$. Here, the accelerating voltage fluctuates around the value set by the pair production threshold. In the bulk of the polar cap, electric field accelerates electrons outwards and pushes positrons inward. As the voltage gets screened by freshly produced pairs, acceleration of the primary particles ceases, and the pair cloud escapes from the discharge zone. We also observe particles leaking from the cloud and propagating back to the star (Timokhin and Arons 2013). In the return current layer, accelerating electric field extracts ions from the stellar surface, which are unable to produce pairs. In this case, electrons, which return back and accelerate toward the star, initiate the discharge. We find that a similar situation happens in the half of the polar cap of the orthogonal rotator, where $\rho_{GJ} > 0$, and ions are extracted. Thus, models with free particle escape are consistent with observations of radio interulses, where both parts of the polar cap are observed to power coherent radio waves.

The most energetic particles in our simulations are ions, extracted from the footpoints of the return current layer, see Figure 4a. Their initial acceleration happens at the base of the return current zone at the edge of the po-

² We are considering the case $\vec{\Omega} \cdot \vec{B} > 0$

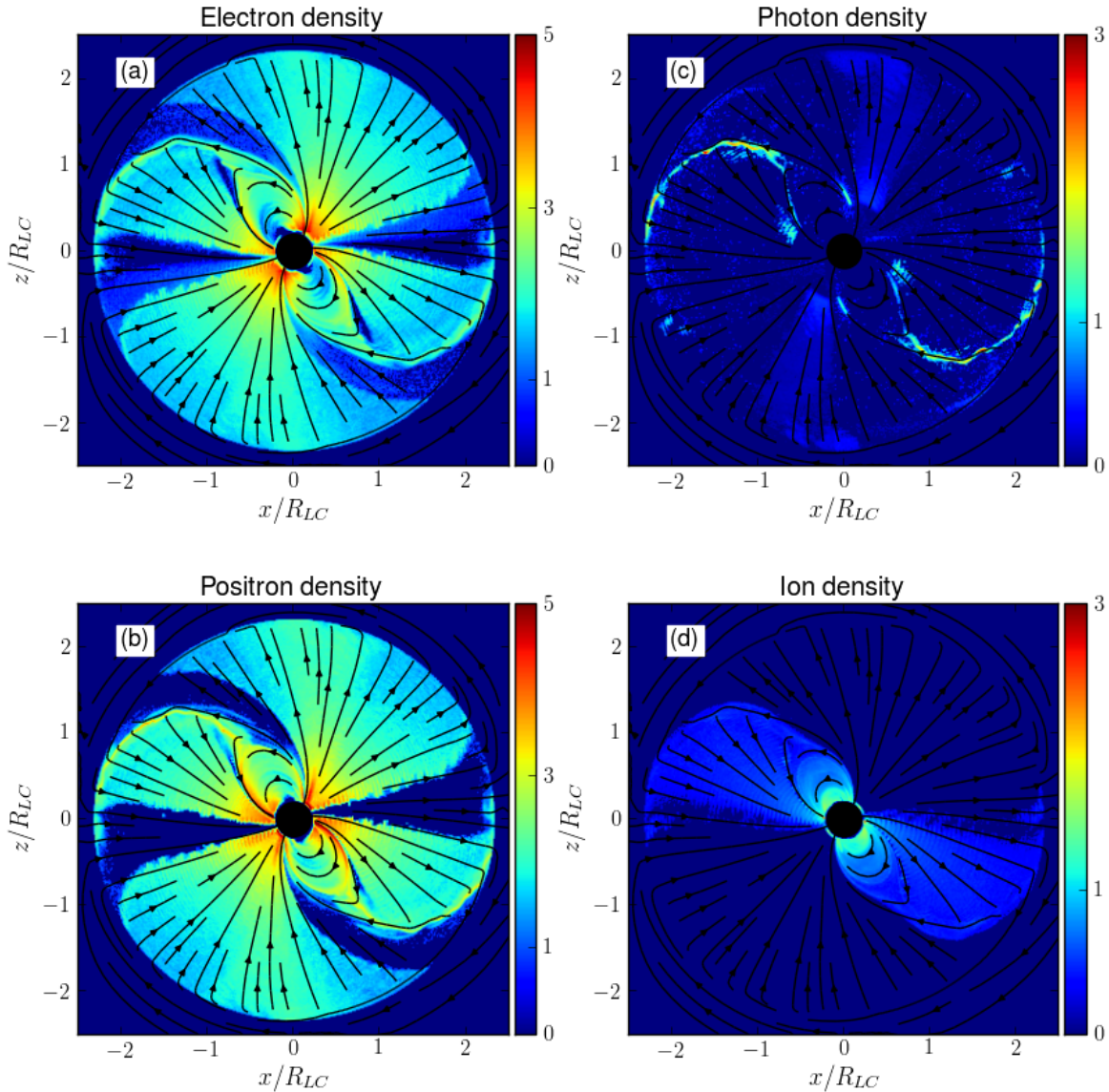


FIG. 1.— Slice through the $\vec{\mu} - \vec{\Omega}_*$ plane for the 60° pulsar magnetosphere. (a): Electron density, (b): positron density, (c): photon density, (d): ion density. Black lines show poloidal magnetic field lines.

lar cap, where e^-/e^+ discharge operates³. However, they gain most of their energy at the Y-point and the current sheet beyond the light cylinder, where $E > B$ occurs. We find that most energetic ions are accelerated close to the equatorial plane. Positrons which reach highest energies in our simulations are created in the e^\pm discharge in the return current sheet, see Figure 4b. They are injected into the Y-point and the current sheet at significantly

³ In the northern part of the polar cap in the northern hemisphere, the return current represents a narrow sheet, which thickness is of order of the plasma skin depth. In the southern part of the polar cap, there is a volume return current zone.

smaller energies compared to ions and experience synchrotron cooling when they encounter strong magnetic field inhomogeneities inside the current sheet. However, their maximum energy is still around σ_{LC} , significantly higher than the limit set by synchrotron radiation reaction. This is because deep inside the current sheet, where $B \rightarrow 0$ and particle acceleration happens, synchrotron losses are significantly reduced and do not limit the particle energy.

In Figure 4c we show different histories of electron energization. The major acceleration region of electrons is the polar cap, as is shown by the trajectory of electron

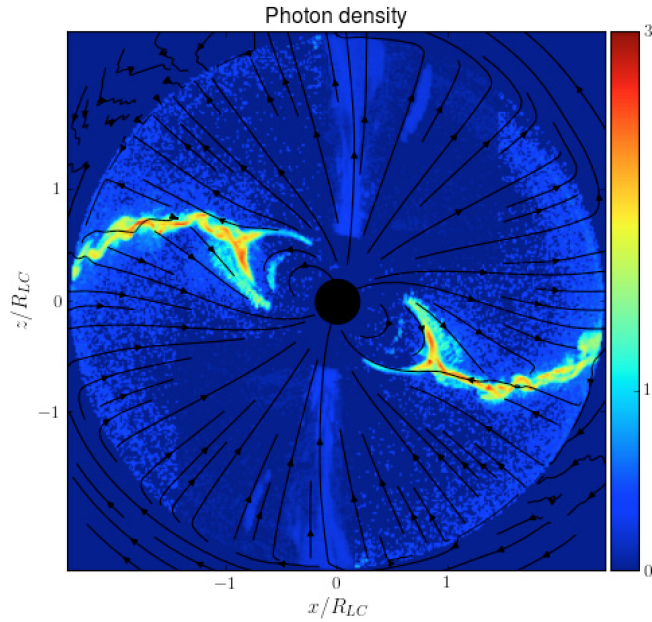


FIG. 2.— High-energy photon density in the magnetosphere of the 30° rotator. Compared to the 60° inclined solution, the return current layer inside the light cylinder is significantly more efficient photon emitter. The kink instability of the current sheet beyond the light cylinder is also more active.

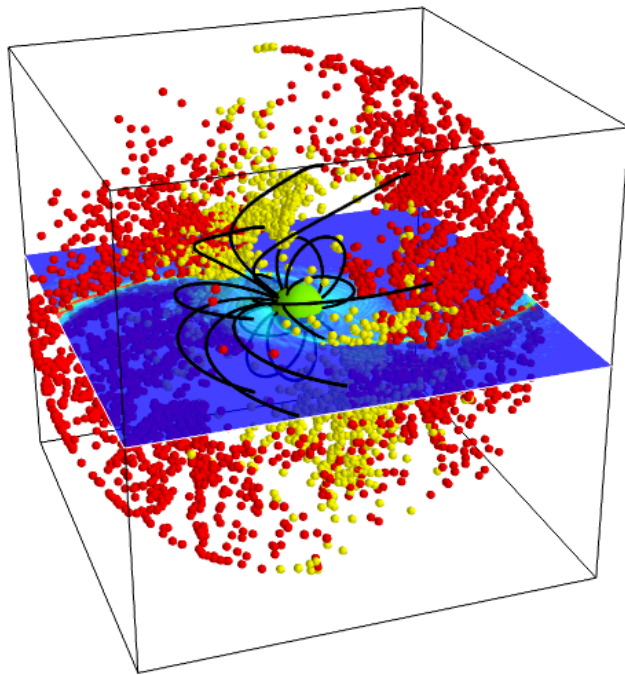


FIG. 3.— Downsamped distribution of high-energy photons in the magnetosphere of 60° inclined pulsar. Red dots show photons propagating outward, and yellow dots show photons, which propagate back to the star. Region near the Y-point contains both photons types. Color in the plane shows the magnetospheric current density.

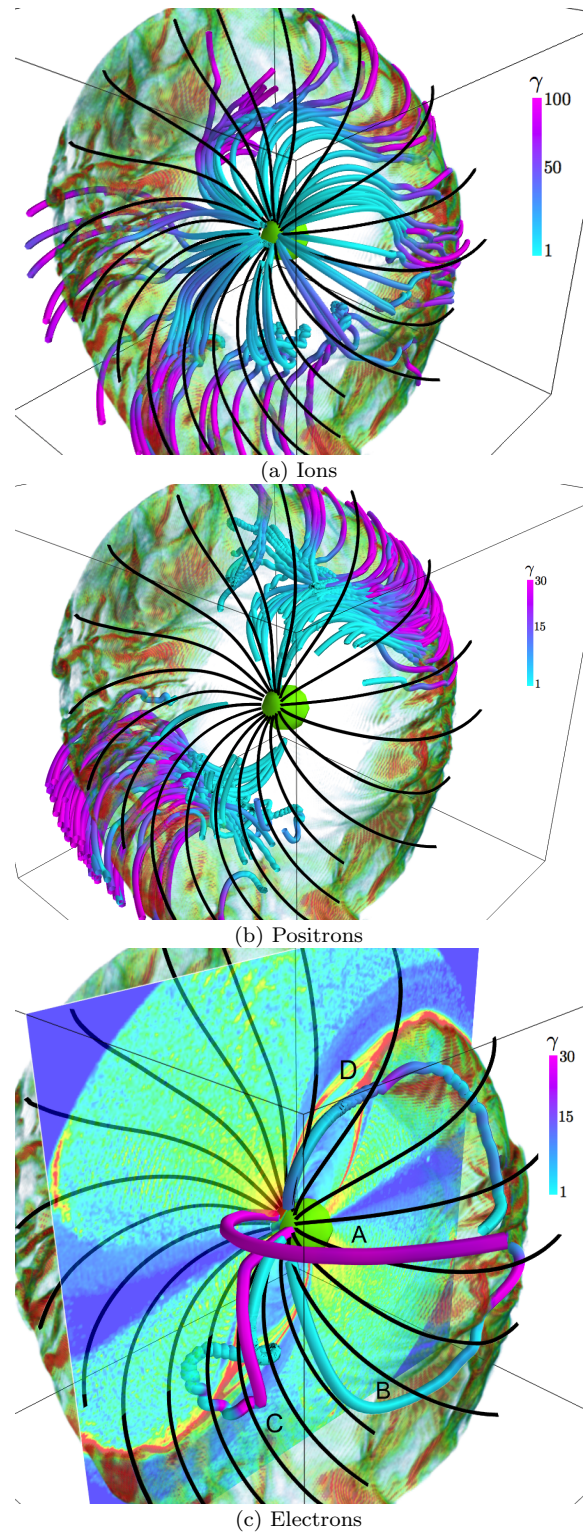


FIG. 4.— 3D trajectories of particles in the corotating frame. Volume rendering shows current density, black lines show magnetic field lines, and colored thick lines show particle trajectories: (a) Ions. (b) Positrons. (c): Electrons. The color of trajectories shows particle's Lorentz factor, with magenta color representing highest energies. Fewer electrons is shown to highlight different types of their trajectories. Color in the plane in panel (c) shows the magnetospheric current density.

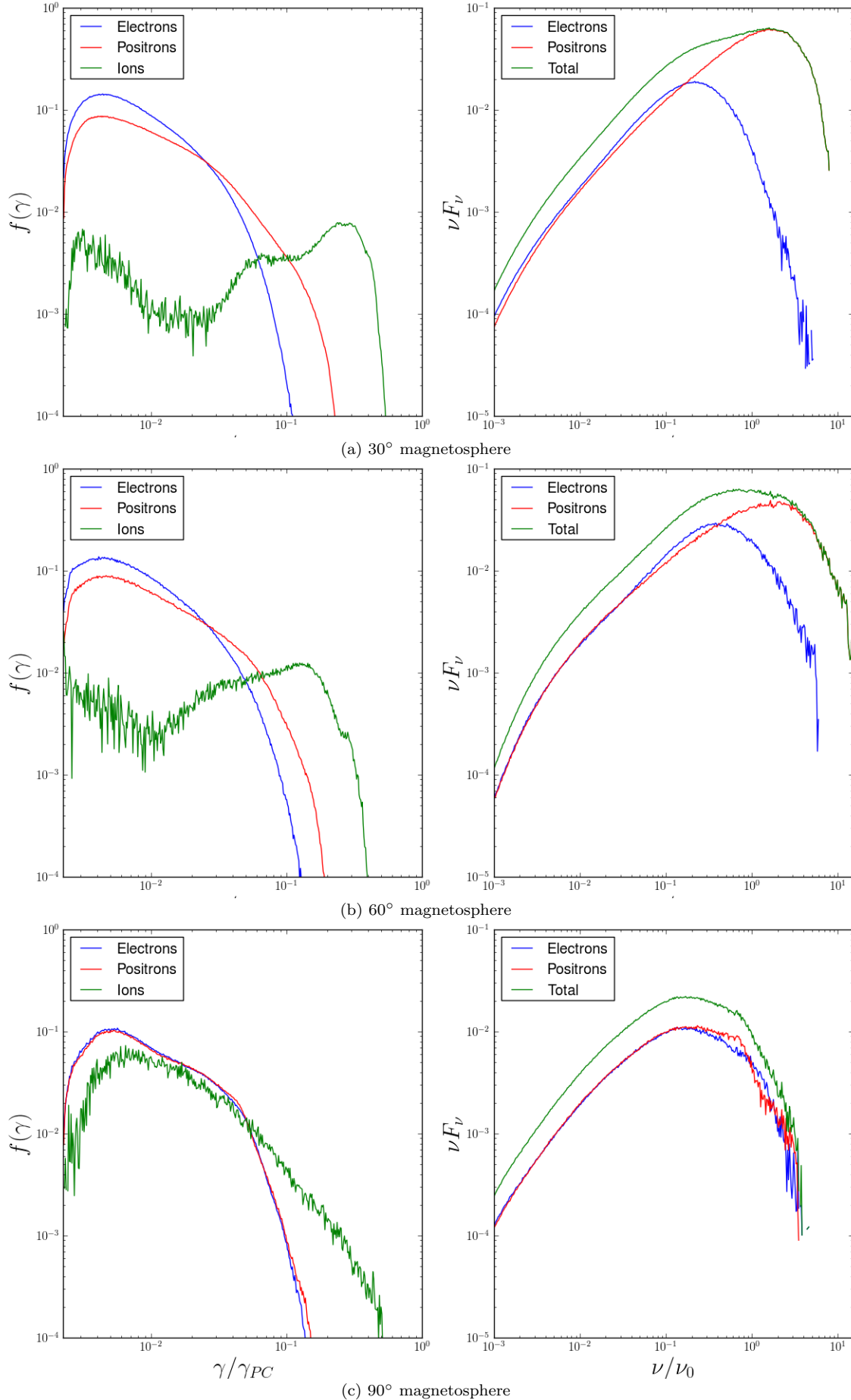


FIG. 5.— Particle and phase-averaged radiation spectrum of the current sheet in the magnetosphere. For particle spectrum, red, blue and green lines represents positrons, electrons and ions, correspondingly. For radiation spectrum, red, blue and green lines represents positron, electron and total emission, correspondingly. The results are shown for a range of inclination angles: (a) 30°, (b) 60°, (c) 90°.

with label A. Here, electrons are accelerated up to the pair formation threshold and initiate the pair discharge, which leads to the screening of the electric field. As in earlier studies, we observe electrons, captured from the wind by the electric field in the current sheet outside the light cylinder, returning back to the star (see trajectory of the electron C in Figure 4c). We also observe some electrons that are produced in the decay of outgoing photons inside the current sheet and reversed by electric field back to the star (see trajectory of the electron D in Figure 4c). Not all electrons are reversed in the current sheet of the oblique rotator. We find that many electrons in the magnetosphere of 60° rotator do significant surfing around the current sheet surface and later reach the equatorial plane, where they are accelerated outwards (trajectory of a representative electron of this sort is labelled as B in Fig.). These electrons contribute to the flux of the high-energy emission.

In Figure 3.1 we show the particle spectrum in the current sheet for different inclinations. Spectrum of electrons and positrons shows a clear power-law tail with index ≈ 1.5 , typical for relativistic magnetic reconnection. The spectrum extends from $\gamma \approx 2$, which corresponds to the injection energy of secondary pairs, until

$$m_e c^2 \sigma_{LC} = B_{LC}(c/\Omega)\lambda = m_e c^2 \gamma_{PC}/\lambda. \quad (2)$$

For low inclination angles, the direction of the electric field in the current sheet does not significantly depend on the distance from the Y-point and is mostly radial. This results in a significant excess of outflowing energetic positrons (Cerutti *et al.* 2015). In current sheets of highly oblique rotators, the electric field is mostly along θ direction. However, close to the Y-point electric field still has a significant radial component, which results in the excess of positrons at highest energies. The peak of the ion energy distribution decreases with increasing inclination angle, being in the range $0.1 - 0.3\Phi_{PC}$.

3.3. Pulsar wind

The structure of the pulsar wind beyond the light cylinder is highly non-uniform. In agreement with earlier conclusions of Tchekhovskoy *et al.* (2016), we find that the Poynting flux is strongly concentrated towards the equator, $\langle S_r \rangle_\phi \approx \sin^4 \theta$, for inclination angles $\alpha > 40^\circ$. More interestingly, we find that plasma density distribution is also very non-uniform. In Figure (a) we show the particle energy flux $\langle n\gamma \rangle$ distribution on a sphere of radius $3R_{LC}$. As is clearly seen, most of the space is filled with plasma, while some regions are mostly empty. The empty regions are connected with two regions. First, there are polar zones around the line $j_\parallel = 0$, which do not launch pair cascades and are sustained by the charge-separated outflow. Second, there is a low density region just above and below the current sheet, first observed in simulations of aligned rotators (Chen and Beloborodov 2014; Philippov *et al.* 2015b). Though including finite mean free path of pair producing photons into account makes the hole filled with plasma, its density is still significantly lower compared to the dense polar outflows and equatorial current sheet. In panel (b) we show the particle flux averaged over azimuth, which coincides with the average over rotational period as the solution is steady in the corotating frame.

Since the wind base conditions are now understood, the long-standing problem of whether the striped pattern of the pulsar wind survives until the termination shock can now be addressed. If our patchy structure extends up to large distances, the non-uniformity of the pulsar wind at its base may have important implications for the particle acceleration at the termination shock. For example, our results imply that σ parameter should be highest at the equator, where particle flux is significantly reduced. If the gap is filled with plasma of density significantly lower compared to the dense polar outflow, the intermediate latitudes may support a high σ region as well.

4. MODELING OF THE HIGH-ENERGY EMISSION

The distribution of photons in Figure 1 shows that the high-energy emission is produced close to the Y-point and in the current sheet. We find that the resulting light curves are similar to PIC simulations without pair production (Cerutti *et al.* 2016), which suggests that the beaming of emission is mainly determined by the magnetospheric geometry rather than by the small-scale plasma processes. In Figure (4) we show the skymaps of high-energy emission for inclination angles $30^\circ, 60^\circ$ and 90° . At low inclination angles, $\alpha < 45^\circ$ the skymap shows a sinusoidal-like caustic, which traces the shape of the current sheet. The caustic is not uniformly bright, showing significant flux enhancement closer to the equator. In this geometry, we expect pulsars produce mainly double-peak gamma-ray emission profiles, most pronounced at viewing angles, $\zeta \approx 90^\circ$. For the intermediate observer's viewing angle $90^\circ < \zeta < 90^\circ \pm \alpha$, double peaks are accompanied by the significant bridge emission (see $\zeta = 100^\circ$ in Figure 4a). For $\zeta \approx \pi/2 \pm \alpha$ single-peaked profiles, centered at $\Phi_P \approx 0.5$, are possible (see $\zeta = 110^\circ$ in Figure 4a). As the inclination angle increases, the two bright equatorial parts become disconnected from each other, see Figure 4b and d. In this case, only the double-peak profiles are expected.

Given everything being equal, the radiative efficiency decreases with the increasing inclination angle, which may partially explain the observed scatter in L_γ vs \dot{E} . The gamma-ray luminosity also depends on the efficiency of the pair production around the light cylinder, which in our setup is parametrized with the mean free path of photons, L_{mfp} . The maximum efficiency corresponds to large $L_{mfp} > 2R_{LC}$, in which case we reproduce the results of (Cerutti *et al.* 2016), where pair production in the current sheet was neglected. In this case only small number of photons is converted into pairs, and the radiative efficiency varies between $\approx 10\%$ for the aligned rotator and $\approx 1\%$ for the orthogonal rotator. As the photon mean free path decreases, pair production becomes more efficient, and the radiative power drops.

Synchrotron emission of the particle distribution in a current layer shows a broad-band spectrum, rising in νF_ν at low energies, see Figure 3.1. The low-energy cutoff of the spectrum is determined by the injection energy of secondary pairs, $\approx B_{LC}\gamma_{sec}^2$, with $\gamma_{sec} \approx 2$. High energy positron excess results in flattening of the emission spectrum at the highest energies. Its peak is at $\nu \approx 0.1B_{LC}\sigma_{LC}^2$, where σ_{LC} takes into account the density of plasma, produced inside the sheet. While the highest energy part of the spectrum shows increasing νF_ν for low inclinations, $< 40^\circ$, it is mostly flat or decreasing

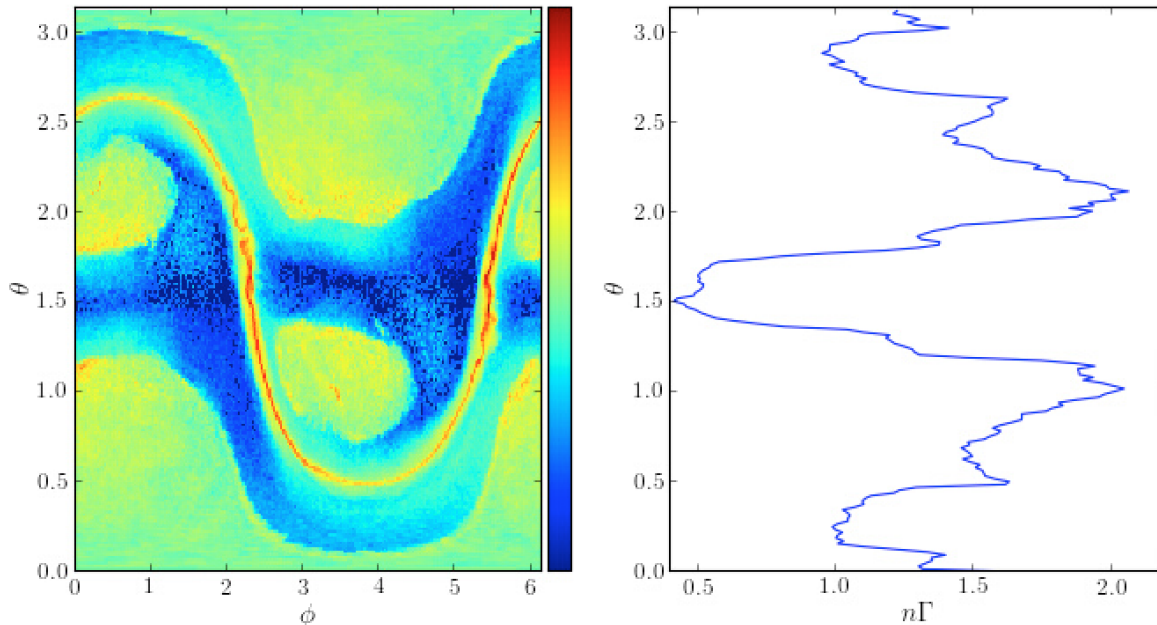


FIG. 6.— (a): Particle flux distribution on a sphere of radius $3R_{LC}$ in a magnetosphere of 60° inclined rotator. (b): Same, but averaged over azimuth. The distribution is highly non-uniform, because pair production does not operate on all field lines.

for larger inclinations. In our simulations we find that the produced plasma multiplicity increases with the increased value of the magnetic field, $\lambda \propto B_{LC}$, so the magnetization parameter σ does not significantly change. Local simulations of pair reconnection with more accurate prescriptions for pair production will be able to identify the dependence of plasma multiplicity cutoff of the high-energy emission spectrum on the magnetic field strength at the light cylinder. We will report this investigation elsewhere.

Pair production in two-photon collisions has the highest cross-section when the center-of-mass energy of colliding photons is around MeV, for example this is satisfied for collisions of GeV and soft X-ray photons. The broadband nature of the radiation spectrum from the current sheet shows that pair-production can be self-sustained, e.g. soft X-ray photons, which are targets for further pair-producing collisions with high-energy GeV photons, are produced by secondary pairs. This should be the case in young active pulsars, like Crab, where the density of X-ray photons is sufficiently high. Older pulsars may sustain an active discharge with X-ray photons from the neutron star surface, similar to outer gap models.

5. DISCUSSION

Our previous study (Philippov *et al.* 2015b) showed that effects of general relativity are essential in driving efficient pair production in aligned pulsars. Here we show that same effects help to increase the fraction of pair producing field lines in magnetospheres of oblique pulsars.

We show that plasma density and the energy flux in the pulsar wind is highly non-uniform. Charge-separated flow on field lines that do not support pair production extends to infinity. Plasma hole above the current sheet, identified previously, is filled with plasma density, much lower compared to the dense polar outflow and the current sheet. Given that wind base conditions are now un-

derstood, σ problem can be addressed from first principles. In particular, it's intriguing to investigate whether the non-uniform striped wind survives until the termination shock, transforms to a vacuum-like wave (Melatos and Melrose 1996) or transitions to turbulence (?).

In agreement with earlier expectations (Cerutti *et al.* 2016), particle acceleration in current sheets is not limited by synchrotron cooling, since energetic particles are focused deep inside the layer, where losses can be neglected. We found that particle acceleration and cutoff of the high-energy emission is regulated by the efficiency of pair production near the Y-point and current sheet. This brings in the new fundamental problem in radiative reconnection research, e.g. how efficient is the pair production in reconnecting current sheets? We will approach this question with local simulations in our future work. Collective motions on plasma scales in the current sheet may power radio counterparts to gamma-ray pulses (and giant pulses).

We find that pulsars are efficient sources of energetic ions. For the geometry $\mathbf{\Omega} \cdot \mathbf{B} > 0$ and inclinations angles not very close to 90° , they are extracted at the base of return current layer. They gain most of their energy at and beyond the Y-point. This is important for reaching extremely high energies, since acceleration in the return layer becomes limited due to curvature radiation losses (Arons 2012). Deep inside the equatorial current sheet, where ions are accelerated, this is not an issue. For parameters of millisecond magnetars, this makes energetic ions interesting candidates for the ultra high-energy cosmic rays.

Previously the concept of "weak pulsar", e.g., a pulsar with sufficiently small magnetic field at the light cylinder to drive efficient pair creation in the outer magnetosphere (Chen and Beloborodov 2014; Gruzinov 2013). We performed axisymmetric simulations with high polar cap voltages and multiplicities of the secondary plasma,

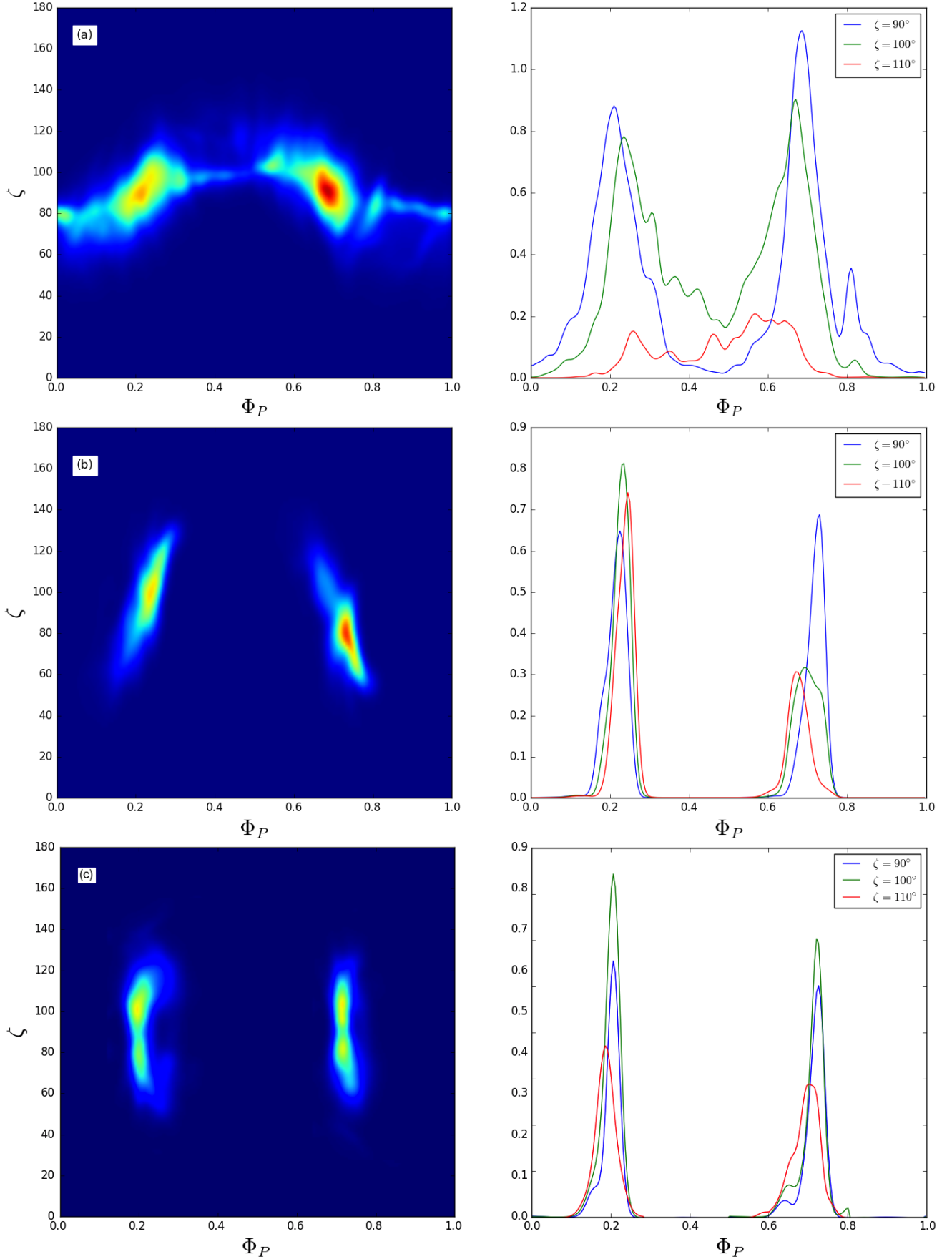


FIG. 7.— Skymaps and lightcurves of the high-energy emission. (a): 30° inclined magnetosphere, (b): 60° inclined magnetosphere, (c): 90° inclined magnetosphere.

and observed the return current being more and more active. We also observe the oscillations between the active force-free like solution and the disk-dome phase, which happens on a timescale of few rotational periods. This can be interesting for modelling nulling in pulsars near the death line, which can not support large multiplicities in their pair cascades. The details will be presented elsewhere.

We thank Jonathan Arons, Andrei Beloborodov, Vasily Beskin, Samuel Gralla, Benoît Cerutti, Andrei Gruzinov, Alexander Tchekhovskoy, and Andrey Timokhin

for fruitful discussions. This research was supported by the NASA Earth and Space Science Fellowship Program (grant NNX15AT50H to AP), Porter Ogden Jacobus Fellowship awarded by Princeton University to AP, NASA grants NNX12AD01G and NNX13AO80G, Simons Foundation (grant 267233 to AS), and was facilitated by Max Planck/Princeton Center for Plasma Physics. The simulations presented in this article used computational resources supported by the PICSciE-OIT High Performance Computing Center and Visualization Laboratory and by NASA/Ames HEC Program (SMD-16-6663, SMD-16-7816).

REFERENCES

- A. A. Philippov and A. Spitkovsky, *ApJ* **785**, L33 (2014), arXiv:1312.4970 [astro-ph.HE].
- A. Y. Chen and A. M. Beloborodov, *ApJ* **795**, L22 (2014).
- M. A. Belyaev, *MNRAS* **449**, 2759 (2015), arXiv:1412.2819 [astro-ph.HE].
- B. Cerutti, A. Philippov, K. Parfrey, and A. Spitkovsky, *MNRAS* **448**, 606 (2015).
- A. A. Philippov, A. Spitkovsky, and B. Cerutti, *ApJ* **801**, L19 (2015a).
- A. A. Philippov, B. Cerutti, A. Tchekhovskoy, and A. Spitkovsky, *ApJ* **815**, L19 (2015b).
- S. E. Gralla, A. Lupsasca, and A. Philippov, ArXiv e-prints (2016), arXiv:1604.04625 [astro-ph.HE].
- M. A. Belyaev and K. Parfrey, ArXiv e-prints (2016), arXiv:1604.05670 [astro-ph.HE].
- B. Cerutti, A. A. Philippov, and A. Spitkovsky, *MNRAS* **457**, 2401 (2016), arXiv:1511.01785 [astro-ph.HE].
- Y. E. Lyubarskii, *A&A* **311**, 172 (1996).
- A. N. Timokhin and J. Arons, *MNRAS* **429**, 20 (2013), arXiv:1206.5819 [astro-ph.HE].
- A. Tchekhovskoy, A. Philippov, and A. Spitkovsky, *MNRAS* **457**, 3384 (2016).
- A. Melatos and D. B. Melrose, *MNRAS* **279**, 1168 (1996).
- J. Arons, *Space Sci. Rev.* **173**, 341 (2012), arXiv:1208.5787 [astro-ph.HE].
- A. Gruzinov, ArXiv e-prints (2013), arXiv:1303.4094 [astro-ph.HE].